J. Fluid Mech. (1977), *vol.* 81, *part* 1, *pp.* 137–154
Printed in Great Britain

Experiments on the structure of turbulence in fully developed pipe flow: interpretation of the measurements by a wave model

By T. R. HEIDRICK, S. BANERJEE
Atomic Energy of Canada Limited, Whiteshell Nuclear Research Establishment, Pinawa, Manitoba, Canada

AND R. S. AZAD
Department of Mechanical Engineering, University of Manitoba, Winnipeg, Manitoba, Canada

(Received 1 December 1975)

This paper is the first of a pair that describe two-point velocity measurements made at various radial positions in water in fully developed pipe flow. Axial velocity fluctuations were measured with hot-film anemometers at two points sufficiently close together that the turbulence structure remained essentially unchanged while passing between them. Phases of the cross-spectra of these velocities were then determined and interpreted in terms of a wave model of the turbulence structure. The model assigns an axial velocity and streamwise inclination to the lines of equal phase of each frequency component of the spectra.

In general, the lines of equal phase for each frequency component are inclined to the wall in the flow direction, the lower frequencies being more inclined than the higher frequencies, though all lines of equal phase at points in the central region of the pipe tend towards the perpendicular. For points near the wall the inclinations are very pronounced.

In the central region, phase velocities of lower frequency components are lower than those for higher frequencies. All phase velocities could be normalized with respect to position by the local mean velocity. The group velocity of small-scale (large wave-number) disturbances in the core region appears to be approximately constant and of the order of the local mean velocity. This leads to a modified form of Taylor's hypothesis.

The variance in all the measurements increases rapidly in the region $y^+ < 26$. This may be due to the intermittent nature of the flow near the wall (which is discussed in part 2) or to a rotation of the 'frozen' pattern by the mean shear field between the two sensors. The magnitude of the latter effect is estimated in this paper and is significant very near the wall. The results in the central region are not affected.

1. Introduction

The earliest models of turbulent shear flows primarily attempted to predict mean flow characteristics in terms of 'universal' parameters. Prandtl (1926) and von Kármán (1931) developed models for calculating the mean velocity field for various flow conditions and geometries. These relationships did not, however, reveal any new information about the character of the turbulence.

The next step was to try to understand and predict quantities related to the turbulence structure. The major effort was devoted to determining how turbulence is maintained. The results of Laufer (1954) illustrated the importance of the region near the wall. Townsend (1956, 1958, 1961), Grant (1958) and more recently Bakewell & Lumley (1967) all tried to characterize the complex motions near the wall in terms of a few prevailing types of eddy. Grant and Townsend both demonstrated that an assumed structure will fit measured correlation functions. The reverse process of inferring a structure from a series of correlation functions is (as noted by Townsend) ambiguous since many different structures can give the same correlation. The space–time correlation measurements of various investigators (summarized up to 1964 by Favre 1965) have provided considerable insight into the types of motion that exist in turbulent shear flows.

The central difficulty in interpreting space–time correlations in shear flows arises because eddies of different sizes may move at different speeds rather than conform to Taylor's (1938) hypothesis that they move at a speed equal to the local average velocity. Thus spectral components of the fluctuating velocity field of different frequency may move past a measuring point at different velocities. The problem of interpretation is made even more difficult, as pointed out by Sternberg (1967), because the disturbances may be inclined to the wall, the degree of inclination being a function of the scale of the motion.

Instead of trying to guess or calculate a dominant structure for near-wall turbulence, Kline and co-workers (Kline *et al.* 1967; Kim, Kline & Reynolds 1968, 1971) observed it visually. These observations showed periods of intense, chaotic activity (called bursts) separated by relatively quiescent periods. Other studies of this intermittent behaviour are reviewed more completely in part 2 of this study. This intermittent behaviour is similar to the dynamic instability observed by several investigators (Martin & Johanson 1965; Klebanoff, Tidstrom & Sargent 1962; Kovasznay, Komoda & Vasuveda 1962) in the laminar-to-turbulent flow transition. The tradition of Fourier analysis of velocity fluctuations and the observed similarity of structure to an instability phenomenon led to travelling-wave representations of the turbulence phenomena. The experiments of Morrison (1969) also suggest that a wave representation of turbulence may be successful.

The wave model of Phillips (1967) proposes a mechanism by which the turbulent components support the Reynolds stress in turbulent shear flows. However, as Phillips noted, the expression obtained is probably not valid near the wall, where the mean vorticity gradient changes rapidly.

Landahl (1967) proposed a model of turbulence where the mean shear flow acts as a waveguide for the disturbance created by the nonlinear breakdown of turbulent eddies. The basic idea introduced is that the turbulent fluctuations in a shear flow may be represented by a superposition of waves of random phase and orientation which are initiated by the interaction of the fluctuating velocities themselves. More recently Lahey & Kline (1971) have shown how the flow-visualization work done at Stanford also suggests a travelling-wave representation. They demonstrated that several 'permissible candidates' for modelling the turbulent fluctuations in terms of travelling waves could lead to the same correlation function. From these comparisons the most promising model was an oblique, non-deterministic wave model with random phase and amplitude. Spectra and correlations in agreement with experiments were

obtained by assuming that the turbulence consisted of these organized parts superimposed on components having no organization.

The preceding discussion was meant to show that a wave representation of the turbulent velocity field may provide insight into the processes which maintain turbulence. A basis for interpreting our experiments in terms of a wave representation is given in the next section. The experiments and results are discussed in § 4. Experimental facilities, techniques, data processing and checks on the validity of the measurements are discussed only briefly in this paper. More detail is available in Heidrick (1974).

The preceding discussion also suggests that a model based on 'averages' may not describe the turbulent processes near the wall owing to the intermittent nature (bursting) of the flow in that region. This intermittent nature was also investigated experimentally, and the results are reported in part 2 of this study.

2. Theoretical basis for interpretation of the experiments

The theoretical basis of a wave model for the axial velocity fluctuations u will be briefly reviewed here. This model assigns an axial velocity and angle of inclination to the wall to the lines of equal phase of each frequency component of the spectrum of u. The mathematical basis for this model is discussed more fully in Heidrick (1974).

The cross-spectral density between axial velocity fluctuations at two points 1 and 2 consists of a real part, the cospectrum $\mathscr{C}(f)$, and an imaginary part, the quadrature $Q(f)$. A measure of the correlation between each frequency component is the coherence

$$R(f) = \left[\frac{\mathscr{C}^2(f)+Q^2(f)}{G_1(f)\,G_2(f)}\right]^{\frac{1}{2}}, \tag{1}$$

where $G_1(f)$ and $G_2(f)$ are the one-dimensional spectra measured at points 1 and 2 respectively.

If the fluctuating signals at points 1 and 2 were identical then $R(f) = 1{\cdot}0$. If the signals were identical except that each spectral frequency component had a relative time shift $\Delta t_{12}(f)$, then not only would the coherence be unity, but also the phase $\theta_{12}(f) = \tan^{-1}(Q(f)/\mathscr{C}(f))$ of the cross-spectrum could be related to $\Delta t_{12}(f)$ by

$$\Delta t_{12}(f) = \theta_{12}(f)/2\pi f. \tag{2}$$

The spectral frequency components at 1 and 2 may be thought of as propagating at different axial velocities $C(f)$. The loci of equal phase of the propagating components may also be inclined with respect to the wall at an angle $\alpha(f)$, as shown in figure 1. The time shift caused by these components as they pass between the measuring points can be determined by measuring the phase of the cross-spectrum and using (2). Although these waves are technically abstractions any wavelike characteristics of the flow should be revealed by an analysis of this type. The two measuring points must, however, be sufficiently close that the coherence $\sim 1{\cdot}0$. For the situation shown in figure 1 (which defines the symbols) the phase shift is related to the disturbance velocity and inclination by

$$\theta_{12}(f) = (2\pi fr/C_1(f))\,[\sin\beta\cot\alpha(f) - \cos\beta] \tag{3}$$

provided that $R(f) \sim 1{\cdot}0$ and $C_1(f)$ and $\alpha(f)$ do not change between the sensors.

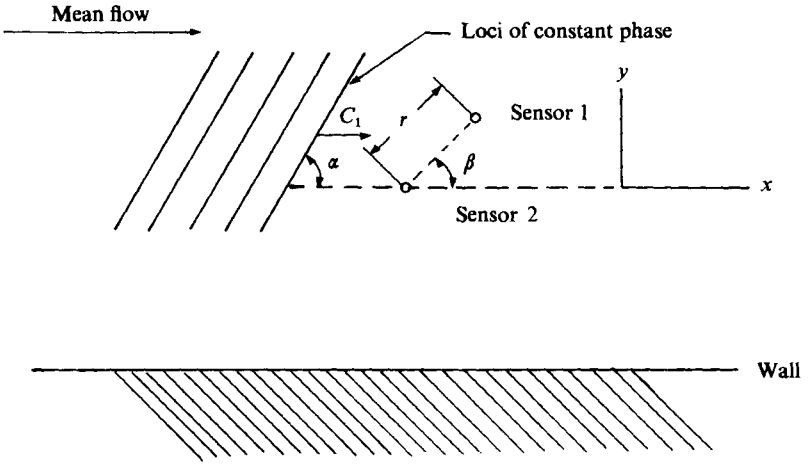

FIGURE 1. Schematic diagram of a disturbance to a 'frozen' pattern in relation to the sensors and the wall. C_1 = phase velocity, α = disturbance inclination.

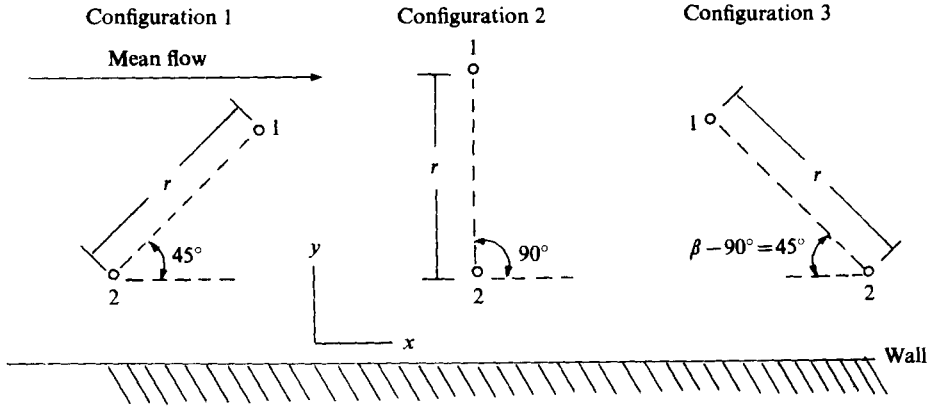

FIGURE 2. Configurations of the two sensor probes used in the study. For configurations 1, 2 and 3, r was 0·254 mm, 0·3048 mm and 0·2032 mm respectively.

Measurement of $\theta_{12}(f)$ with sensor configurations having two different values of β, such as any two of the three in figure 2, allows (3) to be solved for the two unknowns, $C_1(f)$ and $\alpha(f)$. The measurements presented in § 4 were taken with the three orientations shown so that $\alpha(f)$ and $C_1(f)$ could be determined in three different ways and hence the results compared.

Even if $R(f) \sim 1{\cdot}0$ and a 'frozen pattern' may be assumed to convect past the two measuring points, there will still be a distribution of phase velocities associated with each frequency component. An average phase velocity can be calculated by the technique discussed but no information about the distribution of phase velocities about the mean can be obtained. This may not be a serious drawback however, since Morrison (1969) has shown that the distribution of phase velocities is quite concentrated about the mean.

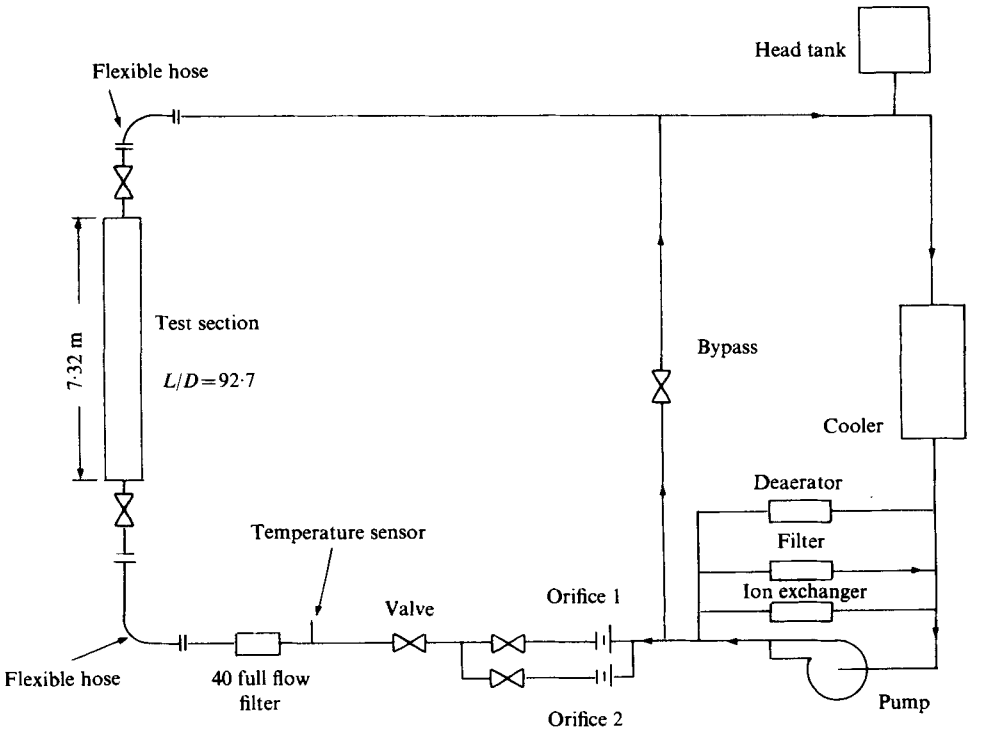

FIGURE 3. Schematic diagram of the experimental apparatus.

3. Experimental equipment and test facility

Experimental loop

The experiments were performed in water ($\nu = 1{\cdot}022$ cS) in a 7·87 cm I.D. round tube that was honed and polished on the inside and inserted into the arrangement shown schematically in figure 3.

The water in the facility was maintained isothermal to within $\pm 0{\cdot}05$ °C by adjusting the cooling rate of the heat exchanger. The head tank was vented to the atmosphere. The test section was a 6·096 m length of nominally 7·79 cm I.D. stainless-steel pipe to which 1·22 m of honed and polished cast aluminium tube was butt-connected. The tubes were of the same diameter to within 0·0711 mm and there was no surface discontinuity at the connexion. The ratio of the length between the entrance and the measuring point to the inside tube diameter was 92·6. Mean velocities $\overline{U}$ were measured at various positions and found to be symmetric. In the log region, they were best represented by Clauser's (1956) equation

$$\overline{U}/U^* = 4{\cdot}9 + 5{\cdot}6 \log (yU^*/\nu), \tag{4}$$

where y is the distance from the wall, U^* is the friction velocity and ν is the kinematic viscosity of the fluid.

Velocity sensors

Velocities were measured with hot-film probes consisting of two sensors (0·0508 mm diameter × 1·67 mm long, 1 mm heated length) placed about 0·25 mm apart in the orientations shown in figure 2. Sensor separations were measured using an optical comparitor and were 0·254, 0·3048 and 0·2032 mm for configurations 1, 2 and 3 respectively. The sensors were separated by about 2–5 Kolmogorov microscales (if the dissipation is estimated from the mean flow variables as in Bakewell & Lumley 1967) for the experiments discussed here. Thus the separation between the two sensors was of the order of the smallest length scales of significance.

An extensive series of experiments was performed to check the effect of one sensor on the other. These experiments were performed in turbulent jets and in turbulent flow through pipes. For example, energy spectral densities, turbulence intensities and amplitude distributions were measured with each sensor. Some of these data are reported in Heidrick, Azad & Banerjee (1972). The spacing between sensors and the orientations were varied. For the range of conditions discussed in this paper, no interference was found between sensors, except for some measurements with the $\beta = 135°$ probe.

The frequency response of the sensors was measured (by the square-wave test) and matched. The response was checked by making the velocities high enough to cause eddy shedding. The vortex shedding frequency was the same for both sensors and in agreement with Roshko (1953).

Anemometers, signal conditioning and data acquisition

The hot-film sensors were calibrated in the measuring section with a Pitot–static tube and the signals were then linearized. A d.c. voltage estimated to be near the mean was subtracted from the signals, which were then low-pass filtered and amplified before being recorded on an analog tape recorder. The electronic and recording circuits for each channel were identical, but their characteristics were checked using sine-wave inputs and a differential phase meter.

Digital data acquisition

The two channels of analog data were digitized simultaneously at either 1000 or 2000 samples/s. Either 1 or 2 min record lengths were accumulated. These digitized data were then processed using the fast Fourier transform algorithm of Cooley & Tukey (1965).

4. Results

Phase velocities and angles of inclination

The phases $\phi_{12}(f)$ of the cross-spectra were measured at various radial positions in the pipe with sensors in the three orientations shown in figure 2. The time delays

$$\Delta t_{12}(f) = \theta_{12}(f)/2\pi f \tag{5}$$

associated with each phase shift were then calculated. A typical example, obtained when the Reynolds number Re_c (based on the pipe radius and centre-line velocity) was 15600, is shown in figure 4.

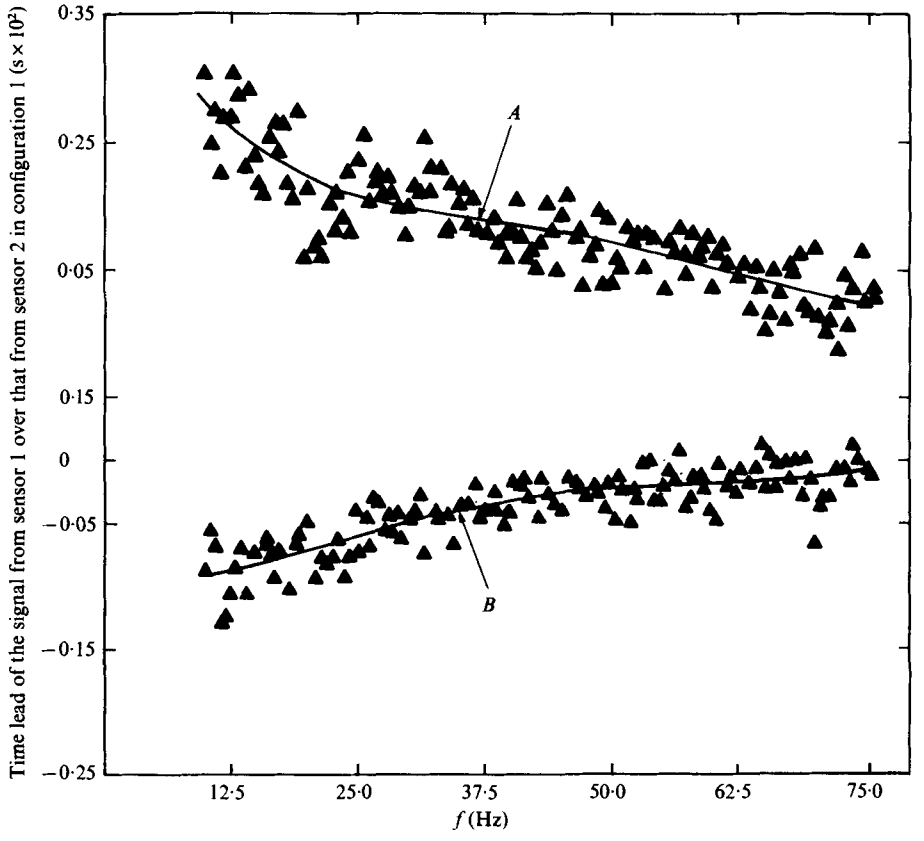

FIGURE 4. Typical time-delay data from a probe in configuration 1 when $Re_c = 15\,600$. The upper curve was measured when sensor 2 was positioned at $y_2^+ = 3{\cdot}89$. The lower curve was measured when $y_2^+ = 26{\cdot}63$. The variance in the data is due to the narrow analysis bandwidth used to ensure an unbiased estimate of the time delay.

The phases of the cross-spectra (and hence the time delays) are subject to random error since they are estimated from finite record lengths. If the signals are Gaussian then the probability p that the true phase lies in the interval $\theta_{12}(f) \pm \Delta\theta_{12}(f)$ is given by Stegen & Van Atta (1970) as

$$\sin^2 \Delta\theta_{12} = \frac{1-R^2}{R^2}[(1-p)^{-2/D} - 1], \tag{6}$$

where D is the number of degrees of freedom in the estimate and is twice the number of realizations for the 'fast Fourier transform' algorithm. R^2 should be the true squared coherence but is replaced by the measured squared coherence to obtain an estimate of $\Delta\theta_{12}$. The coherence is relatively constant at low frequencies and the phase decreases towards $\theta_{12}(f) = 0$. Hence there is a frequency below which $\theta_{12}(f)$ and $\Delta\theta_{12}(f)$ are of comparable magnitude. This frequency is a lower bound on the range of frequencies where one can have confidence in the measurements of $\theta_{12}(f)$ or $\Delta t_{12}(f)$. The number of degrees of freedom used for all the low frequency results was 126. For $R^2 = 0{\cdot}90$ this yields 95 % confidence limits on the measured phase of 4·2°. At 10 Hz this 4·2° corresponds to a time shift of 5·56 ms.

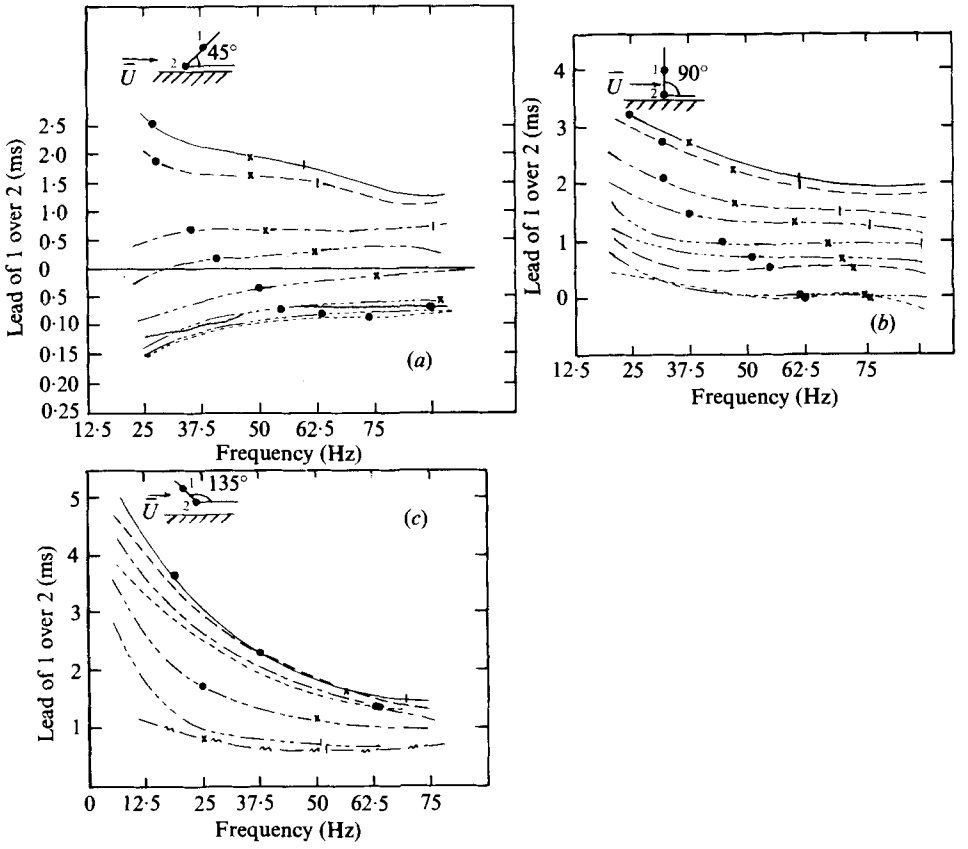

FIGURE 5. Time delays measured with various probes when $Re_c = 15600$. ●, frequency at which squared coherence is 0·9 at each position; ×, frequency at which squared coherence is 0·8; |, frequency where squared coherence is 0·7. (*a*) ——, $y_2^+ = 3{\cdot}89$; – –, $y_2^+ = 8{\cdot}95$; –·–, $y_2^+ = 12{\cdot}95$; –··–, $y_2^+ = 17{\cdot}59$; –····–, $y_2^+ = 26{\cdot}63$; –·····–, $y_2^+ = 44{\cdot}38$; –·····–, $y = 72, y/R = 0{\cdot}1023$; ·····, $y/R = 1525$; wwww, $y/R = 1$. (*b*) —, $y_2^+ = 9{\cdot}5$; – –, $y_2^+ = 6{\cdot}8$; –·–, $y_2^+ = 11{\cdot}5$; –··–, $y_2^+ = 15{\cdot}9$; –····–, $y/R = 0{\cdot}0355$; – – –, $y/R = 0{\cdot}0484$; – – –, $y/R = 0{\cdot}0613$; ·····, $y/R = 0{\cdot}75$; ·····, $y/R = 1{\cdot}0$. (*c*) ——, $y_2^+ = 2{\cdot}86$; – –, $y_2^+ = 5{\cdot}3$; ———, $y_2^+ = 11{\cdot}95$; ·····, $y/R = 0{\cdot}164$; –····–, $y/R = 0{\cdot}75$; – –, $y/R = 1{\cdot}0$.

Results for $Re_c = 15600$

Since the data from each probe configuration were not taken at identical radial positions in the pipe, it was necessary to interpolate between the results to obtain values of $C_1(f)$ and $\alpha(f)$ from (3). For this purpose each set of data was least-squares fitted by a polynomial. For example, the lines shown in figure 4 are fits to the data shown. Figure 5 summarizes the time delays measured when $Re_c = 15600$. Also indicated on these curves are several values of the square of the coherence (R^2) as this is a measure of the variability in the phase data. The coherence is generally higher at points closest to the centre of the pipe, though the coherence measured with the $\beta = 135°$ probe appears to be lower at the centre of the pipe. However, this exception is probably due to the decreasing signal/noise ratio measured with this probe as it was traversed towards the centre of the pipe since an increased noise level will cause a decrease in the measured coherence.

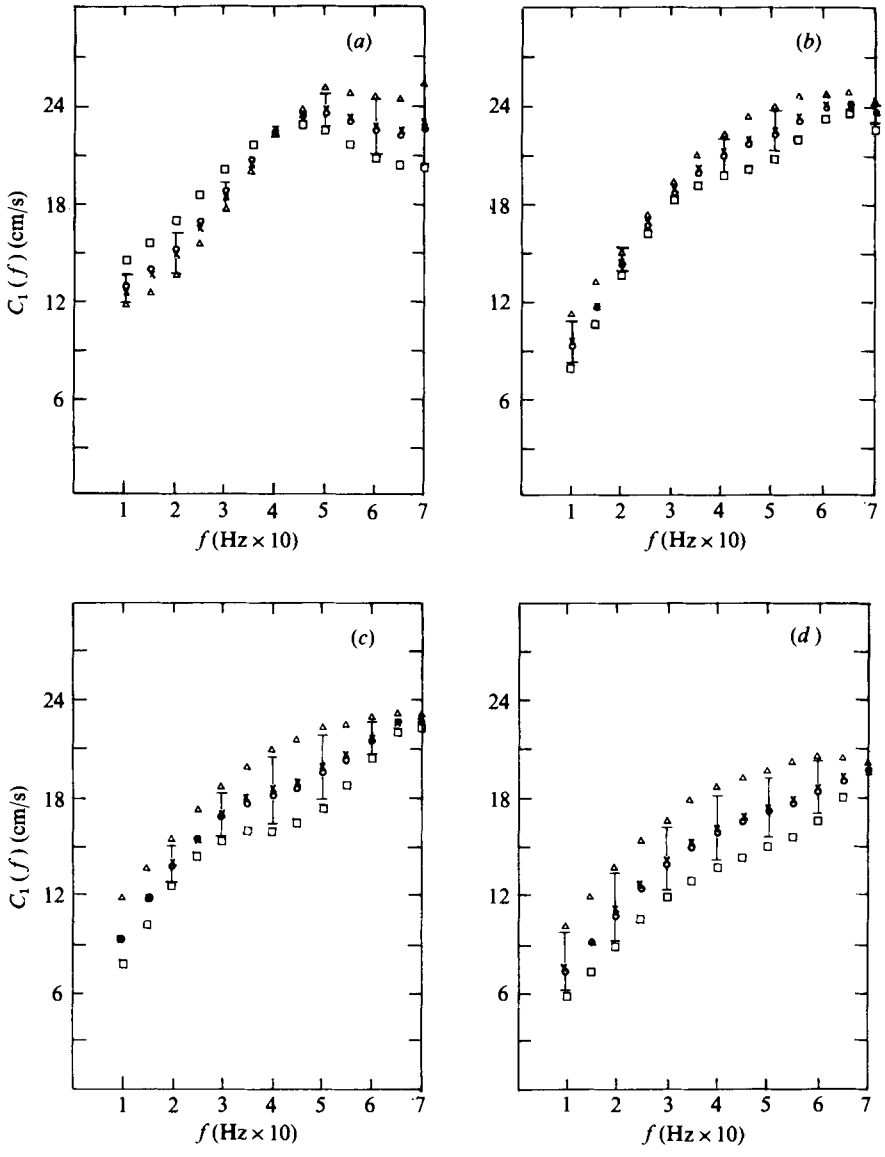

FIGURE 6. Phase velocities when $Re_c = 15600$ for (*a*) $y/R = 1$, (*b*) $y/R = 0{\cdot}75$, (*c*) $y/R = 0{\cdot}5$ and (*d*) $y/R = 0{\cdot}25$. The different symbols indicate the sensor combinations used to solve (2): □, 90° and 135° probes; ●, 45° and 135° probes; △, 45° and 90° probes; ×, least-squares fit.

Time delays were taken from figure 5, interpolated to identical radial positions (values of y) and then converted to the phase velocities and angles of inclination defined by (2). Figures 6 and 7 show the phase velocities calculated in this manner using various probe combinations. If the time-delay measurements were perfect, then the values of $C_1(f)$ calculated with each combination (pair of configurations) would be identical. However, it is apparent that the results do not totally agree. Agreement between the results calculated from different sensor pairs is fairly good for $y/R > 0{\cdot}06$. However, the agreement closer to the wall (where the general coherence level is lower)

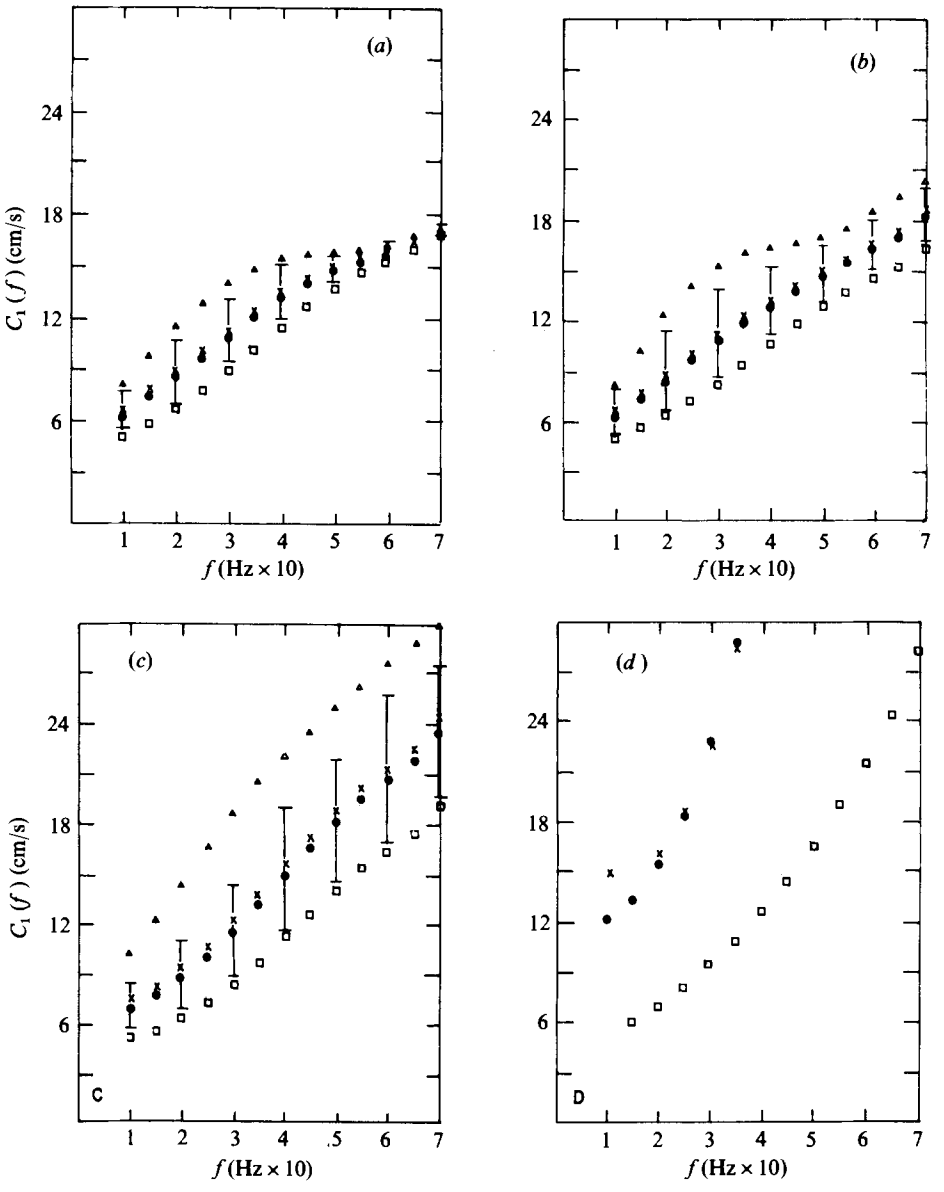

FIGURE 7. Phase velocities when $Re_c = 15600$ for (*a*) $y/R = 0{\cdot}1023$, $y^+ = 72$, (*b*) $y/R = 0{\cdot}063$, $y^+ = 44{\cdot}38$, (*c*) $y/R = 0{\cdot}0355$, $y^+ = 25{\cdot}01$ and (*d*) $y/R = 0{\cdot}012$, $y^+ = 8{\cdot}45$. Symbols as in figure 6;

is not good. If flow near the wall is made up of intermittent intervals of quasi-periodic behaviour interspersed with background turbulence then the present wave model based on 'averages' might be expected to break down near the wall.

As previously noted, the model also relies on $C_1(f)$ and $\alpha(f)$ being constant between the sensors. Near the wall, each frequency component (depicted in figure 1) may undergo a significant amount of rotation owing to the steep velocity gradient. Hence the assumption of a constant $\alpha(f)$ becomes less useful near the wall: a rotational component has to be added to the model. This effect is discussed in the appendix,

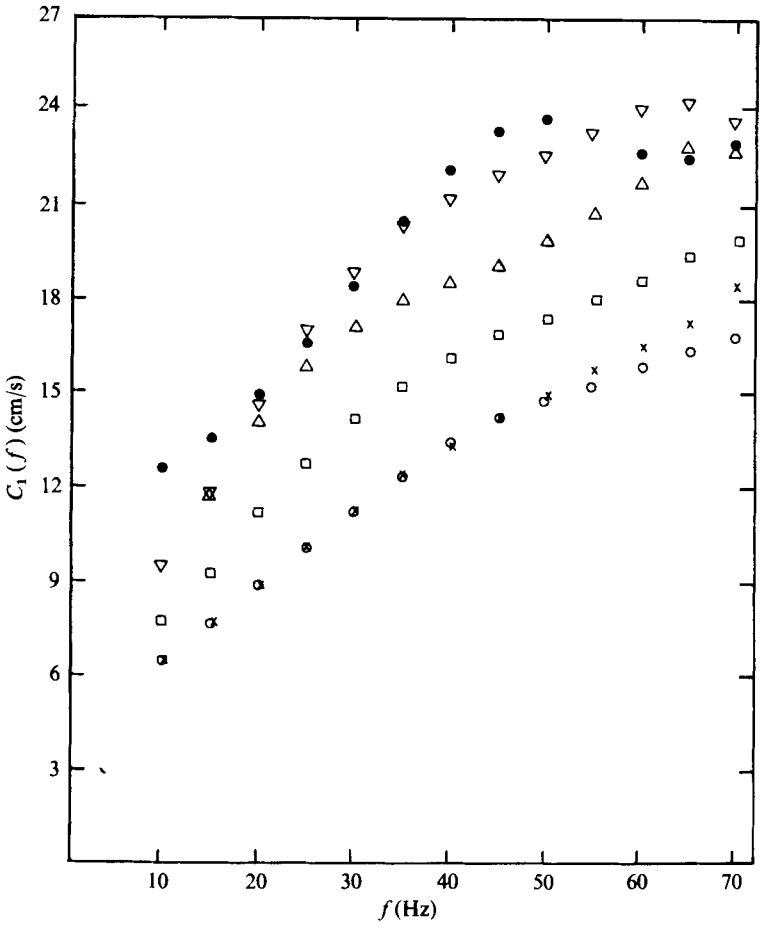

FIGURE 8. Summary of phase velocities in turbulent pipe flow at $Re_c = 15600$. ×, $y/R = 0{\cdot}063$, $y^+ = 44{\cdot}4$; ○, $y/R = 0{\cdot}1023$, $y^+ = 72$; □, $y/R = 0{\cdot}251$; △, $y/R = 0{\cdot}501$; ▽, $y/R = 0{\cdot}75$; ●, $y/R = 1{\cdot}0$.

where it is shown that the applicability of the simple model is affected. The effect is, however, small for positions in the central region of the pipe.

Since each measurement of the time delay is subject to some error, a 'best estimate' of $C_1(f)$ and $\alpha(f)$ can be chosen to minimize the total error in the measured time delays. The data were processed with a computer program (Shih 1968) to select the values of $C_1(f)$ and $\alpha(f)$ that minimized the least-square deviation of the measured time delays from the best values for the time delays. These results are also indicated in figures 6 and 7. The difference in results obtained with the various sensor combinations is indicated by the standard error bars shown on alternate data points.

The 'best estimates' of $C_1(f)$ at various central positions are summarized in figure 8 as a function of frequency. For clarity, the error bars have not been included but are shown in the previous figures.

Two general conclusions are evident from figure 8.

(i) The lower frequency components propagate more slowly than those of higher frequency.

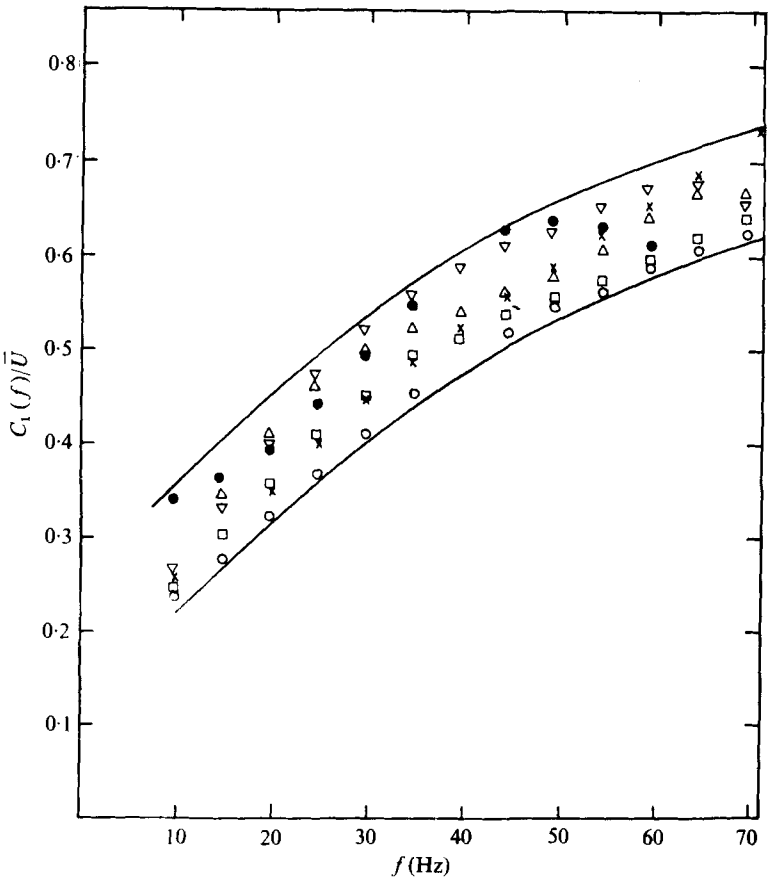

FIGURE 9. Phase velocities normalized by the local mean velocity at various positions in the core region of fully developed pipe flow at $Re_c = 15\,600$. Symbols as in figure 8.

(ii) As the centre of the pipe is approached, the phase velocities increase in a manner similar to the mean velocity.

In figure 9, $C_1(f)$ normalized by the local mean velocity is plotted against frequency for various positions in the pipe. The scatter appears to be reduced at the lower frequencies. The second conclusion is again supported.

The best estimates of the angles of inclination ($\alpha(f)$ in figure 2) of the loci of equal phase for the frequency components are plotted against frequency in figure 10 for various radial positions. The conclusions regarding the loci of equal phase for the frequency components are as follows.

(i) They make smaller angles with the wall (are more sharply inclined) for positions closer to the wall.

(ii) They are more sharply inclined for the lower frequencies than for the higher frequencies.

(iii) For the higher frequencies they are perpendicular to the wall near the centre of the pipe.

(iv) They tend to reach the same inclinations at all radial positions for the lower frequencies.

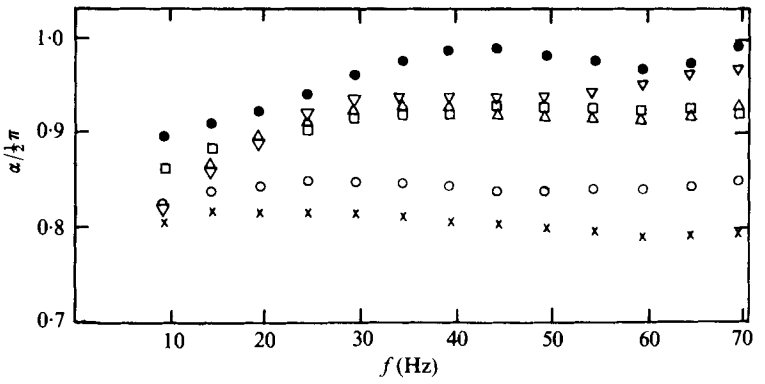

FIGURE 10. Angles of inclination (normalized by $\frac{1}{2}\pi$) of the frequency components of u in the core region of fully developed pipe flow at $Re_c = 15600$. Symbols as figure 8.

The last conclusion is explainable in physical terms because large-scale structures might extend across all or most of the positions shown and have a dominant angle of inclination. This would explain why the lower frequency components tend to be equally inclined to the wall irrespective of distance from the wall. In figure 8, a similar but less discernible trend is evident at low frequencies for $C_1(f)$; at the low frequencies the phase velocities tend to the same value for all distances from the wall.

Phase-velocity/frequency data have been replotted in terms of the radial frequency ω and radial wavenumber $k = \omega/C_1$ in figure 11. This plot permits the determination of a 'group velocity'. It is difficult (Brillouin 1960, p. 97) to define a 'group velocity' physically except in simple circumstances, though it is simple to define mathematically. The definition arises from considering two waves $A\cos(\omega_1 t - k_1 x)$ and $A\cos(\omega_2 t - k_2 x)$, which are superimposed to give

$$\psi = A\cos(\omega_1 t - k_1 x) + A\cos(\omega_2 t - k_2 x).$$

If the waves have quite similar characteristics, i.e.

$$\omega_1 = \omega + \Delta\omega, \quad k_1 = k + \Delta k, \quad \omega_2 = \omega - \Delta\omega, \quad k_2 = k - \Delta k,$$

then (5) becomes

$$\psi = 2A\cos(\Delta\omega t - \Delta k)\cos(\omega t - k). \tag{7}$$

This is a carrier with frequency ω_1 and a modulation with frequency $\Delta\omega$. Thus the wave may be described as a series of moving beats (or groups or wave packets). The phase velocity is the velocity of the carrier, i.e.

$$C \equiv \omega/k. \tag{8}$$

The group velocity is the velocity of the wave packets, i.e.

$$U_g \equiv \Delta\omega/\Delta k \to \partial\omega/\partial k \quad \text{as} \quad \Delta k \to 0. \tag{9}$$

Physically, U_g is the velocity of the wave packets formed by the superposition of the individual waves. When the data are plotted as in figure 11 then the phase velocity $C_1(\omega)$ is given by the slope of the straight line joining the origin to the point on the curve at the frequency ω [from (8)]. The group velocity at ω is the slope of the tangent to the curve at ω [from (9)].

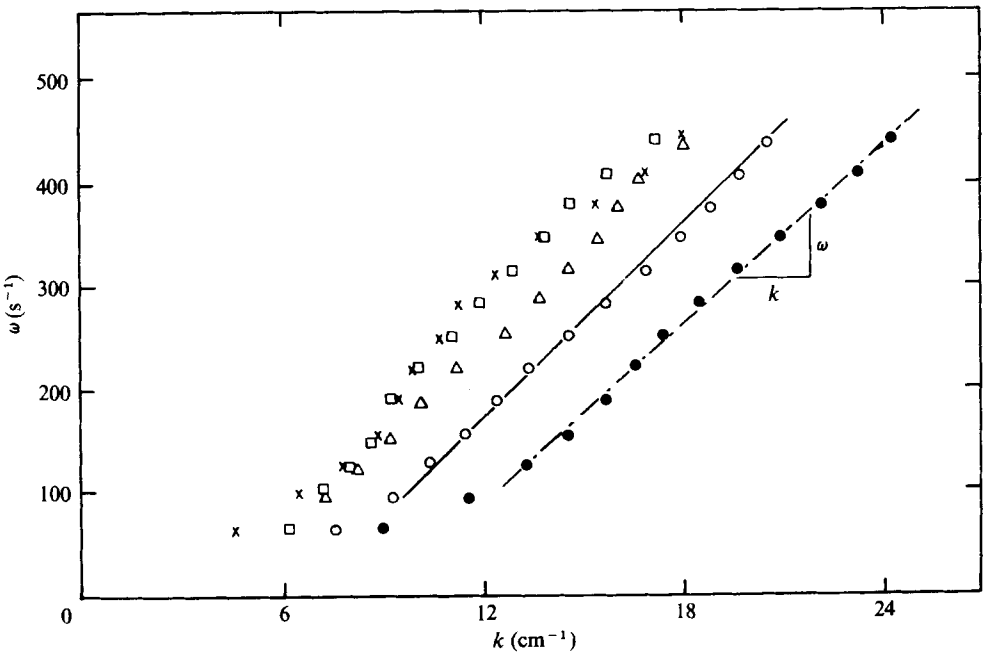

FIGURE 11. Radial frequency ω *vs.* wavenumber k at various positions when $Re_c = 15\,600$. ●, $y/R = 0{\cdot}1023$, $y^+ = 72$; ○, $y/R = 0{\cdot}251$; △, $y/R = 0{\cdot}501$; □, $y/R = 0{\cdot}75$; ×, $y/R = 1{\cdot}0$; – – –, $U_g \equiv \partial\omega/\partial k = U_{\text{local}} = 27{\cdot}98$ cm/s; ——, $U_g = U_{\text{local}} = 32{\cdot}0$ cm/s.

At the higher wavenumbers in figure 11 the group velocity is constant and equal to the local mean velocity at positions with $y/R = 0{\cdot}1023$ and $0{\cdot}25$. The scatter in the data becomes larger as the centre of the pipe is approached, and it is difficult to determine whether the group velocity is equal to the local mean velocity $\overline{U}$. However the slopes of the curves do increase (as they would if $\overline{U} = U_g$) and it appears certain that the group velocity is near the mean velocity for $k > 12\,\text{cm}^{-1}$ at positions in the core region of the pipe. The slopes of the best straight-line fits to this region of k for $y/R > 0{\cdot}5$ are actually somewhat less than $\overline{U}$ for each case, but no firm conclusions can be drawn because of the scatter.

For situations where ω and k are linearly related, as for the higher wavenumbers in figure 11, it can be shown (Brillouin 1960, p. 10) that the modulations or groups propagate without distortion. Thus, since the kth wavenumber component of u is the recombination of several wavenumber components (i.e. the 'group') this actually implies a modified frozen-pattern hypothesis; that is, the smaller scales ($k > 12\,\text{cm}^{-1}$) in the central region ($y/R > 0{\cdot}1$) of fully developed pipe flow convect in a frozen pattern at a group velocity close to the local mean velocity.

A data analysis similar to that discussed in the previous section was performed for a more restricted range of radial positions for measurements made at Reynolds numbers of 33 000 and 63 900 (for details see Heidrick 1974). The general behaviour of all the quantities discussed above was similar, with a few exceptions for the highest Reynolds number. For this case the time delays measured were very small since the flow velocity was high. The phase velocities and inclinations showed reasonable agreement with the other measurements at high frequencies, but rather high phase velocities were found

at low frequencies. This inconsistency was probably due to the very small time delays which had to be measured.

Also, a lower fraction of the total turbulence kinetic energy is held in the low frequency components for two highest Reynolds numbers. This results in a decreased signal/noise level at low frequencies compared with the tests at lower Reynolds numbers.

In the ω *vs.* k plot (similar to figure 11) for the tests with $Re_c = 63\,900$, a maximum wavenumber appeared to be attained for each position. A cut-off of this sort is physically necessary because there will be a finite lower limit to the size of the eddies in the turbulent flow. The physical dimension corresponding to the cut-off wavenumber ranges from 0·0024 to 0·0036 cm.

5. Summary and conclusions

In the central region of the pipe, $y^+ > 30$, the spectral frequency components behave similarly at all the Reynolds numbers investigated, except for some inconsistencies for the highest Reynolds number.

In general, the phase velocities of the components are less than the local mean velocity in the central region. The lower frequency components propagate more slowly than those of higher frequency. Phase velocities at all frequencies increase with distance from the wall, however the lowest frequency components tend to propagate at the same velocity throughout the central region.

The loci of equal phase for the frequency components are more sharply inclined in the flow direction (i.e. $\alpha(f)$ decreases) as the wall is approached. The lower frequencies are more inclined than the higher, which become perpendicular near the centre of the pipe. In the central region, inclinations at the lowest frequencies tend towards the same value. The group velocities at the smaller scales (higher wavenumbers), calculated from the phase velocities, were near the local mean velocity in the central region. This suggests a modified form of Taylor's hypothesis.

Difficulties were encountered in interpreting the results for the near-wall region ($y^+ < 30$) in this way. This may be due to either rotational effects of the mean shear field or the intermittent nature of the flow near the wall. Recent visual studies (Kim *et al.* 1971; Kline *et al.* 1967) have shown that the near-wall region consists of two distinct types of motion: (*a*) a quasi-periodic motion and (*b*) a more random type of background turbulence. Hence the statistical behaviour of $u(t)$ during motion of type (*a*) may be completely different from that during motion of type (*b*). Thus a quantity averaged over both types of interval may be inadequate. Further work has been undertaken to provide insight into how the intermittent intervals of quasi-periodic activity in the wall region affect the structure of the flow near the wall.

Appendix. The effects of rotation on the decomposition of the measured wave

An estimate of the effects of rotation may be obtained by considering figure 12. As the frequency component passes from sensor 1 to sensor 2 it rotates owing to a relative velocity between the top and bottom. The equation relating the measured phase shift, phase velocity and inclination [analogous to (3)] is

$$\theta_{12}(f) = \frac{2\pi f r}{C_1(f) + \Delta u} (\sin\beta \cot\alpha' - \cos\beta). \tag{A 1}$$

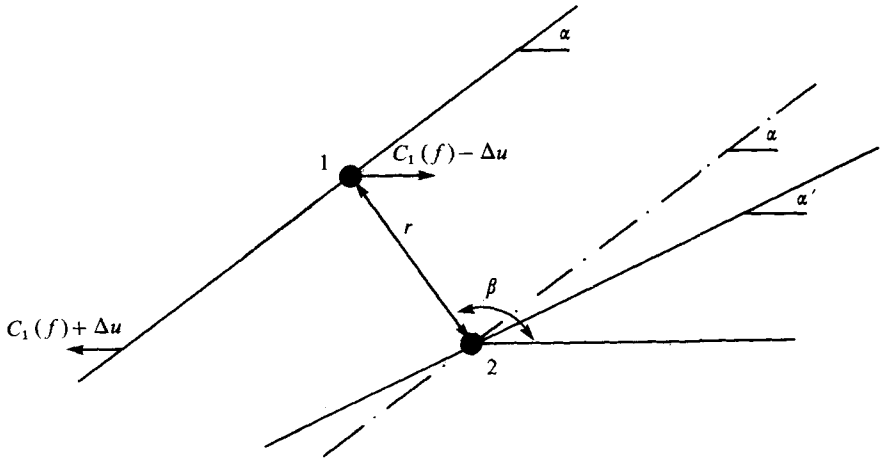

FIGURE 12. Schematic diagram of a locus of constant phase translating and rotating as it passes between two sensors.

If this relative velocity is caused by the mean velocity gradient then

$$\Delta u = \tfrac{1}{2} r \sin\beta \, \delta U/\delta y$$

and thus

$$\theta_{12}(f) = \frac{2\pi f r}{\tfrac{1}{2} C_1(f)\, r \sin\beta \, \delta U/\delta y} (\sin\beta \cot\alpha' - \cos\beta).$$

An expression may be written down for each sensor of figure 2 by substituting the appropriate dimensions:

$$\theta^1_{12}(f) = \frac{2{\cdot}54 \times 10^{-4}(2\pi f)}{C_1(f) + 8{\cdot}96 \times 10^{-5}\, \delta U/\delta y} (0{\cdot}707 \cot\alpha' - 0{\cdot}707), \tag{A 2}$$

$$\theta^2_{12}(f) = \frac{3{\cdot}048 \times 10^{-4}(2\pi f)}{C_1(f) + 1{\cdot}524 \times 10^{-4}\, \delta U/\delta y} \cot\alpha', \tag{A 3}$$

$$\theta^3_{12}(f) = \frac{2{\cdot}032 \times 10^{-4}(2\pi f)}{C_1(f) + 7{\cdot}19 \times 10^{-5}\, \delta U/\delta y} (0{\cdot}707 \cot\alpha' + 0{\cdot}707). \tag{A 4}$$

The units for $C_1(f)$ and U in these expressions are m/s. A superscript denotes the configuration number from figure 2. These expressions could also be written in terms of the inclination α instead of α' by substituting

$$\cot\alpha' = \cot\alpha + \frac{1}{2(2\pi f)} \frac{\delta U}{\delta y}.$$

To solve any pair of these equations (or the equivalent pair using α) we have to assume either that α or that α' is the same for each pair of probes. However, it can be shown that using either assumption results in the same final expression for $C_1(f)$.

Solving (A 2) and (A 3) yields the following expression for $C_1(f)$:

$$C_1(f) = \frac{0{\cdot}589 \times 10^{-4}(2\pi f)}{0{\cdot}589\theta^2_{12}(f) - \theta^1_{12}(f)} + \frac{8{\cdot}96 \times 10^{-5}\, (\delta U/\delta y)\, (\theta^1_{12}(f) - \theta^2_{12}(f))}{0{\cdot}589\theta^2_{12}(f) - \theta^1_{12}(f)}. \tag{A 5}$$

The first term is identical with the solution of (2) for these sensors, and the second term is the correction to $C_1(f)$ for rotational effects. Denoting the above type of solution

as $C^{12}_{\text{rot}}(f)$ and the solution to (2) as $C^{12}_{\text{no rot}}(f)$ (where the superscript denotes the pair of sensors), each pair out of (A 2)–(A 4) may be solved, yielding

$$C^{23}_{\text{rot}}(f) = C^{23}_{\text{no rot}}(f) + \frac{7{\cdot}19 \times 10^{-5}(\delta U/\delta y)\,(\theta^2_{12}(f) - \theta^3_{12}(f))}{\theta^3_{12}(f) - 0{\cdot}472\theta^2_{12}(f)}, \tag{A 6}$$

$$C^{12}_{\text{rot}}(f) = C^{12}_{\text{no rot}}(f) + \frac{8{\cdot}96 \times 10^{-5}(\delta U/\delta y)\,(\theta^1_{12}(f) - \theta^2_{12}(f))}{0{\cdot}589\theta^2_{12}(f) - \theta^1_{12}(f)}, \tag{A 7}$$

$$C^{13}_{\text{rot}}(f) = C^{13}_{\text{no rot}}(f) + \frac{7{\cdot}19 \times 10^{-5}(\delta U/\delta y)\,(\theta^1_{12}(f) - \theta^3_{12}(f))}{\theta^3_{12}(f) - 0{\cdot}8\theta^1_{12}(f)}. \tag{A 8}$$

These expressions may now be used to investigate the order of magnitude of the effects of rotation. For example, at $y^+ \sim 26$, where $\theta^1_{12}(f) = 0$, the rotational corrections to $C_{\text{no rot}}(f)$ that are calculated from (A 7) and (A 8) are independent of frequency and easily estimated. At $y^+ \sim 26$, (A 7) becomes

$$C^{12}_{\text{rot}}(f) = C^{12}_{\text{no rot}}(f) - 4{\cdot}6 \times 10^{-3}\,\text{m/s}$$

and (A 8) becomes

$$C^{13}_{\text{rot}}(f) = C^{13}_{\text{no rot}}(f) - 2{\cdot}2 \times 10^{-3}\,\text{m/s}.$$

The order of magnitude of the correction to $C^{13}_{\text{no rot}}(f)$, $C^{12}_{\text{no rot}}(f)$ or $C^{13}_{\text{no rot}}(f)$ is thus not large enough to explain the increasing scatter visible in the data shown in figure 7 at $y^+ \sim 26$.

At $y^+ > 26$ the magnitudes of the corrections to each phase-velocity equation can be shown to be about equal by substituting several typical values into (A 6)–(A 8). Hence the validity of least-squares fitting the data to obtain the best estimate of $C_1(f)$ is not affected by a rotational correction in this region of the flow.

For positions closer to the wall than $y^+ \sim 26$, (A 5) and (A 7) reveal that both $C^{12}_{\text{no rot}}$ and the correction to it for rotation are extremely sensitive to the measured values of $\theta^1_{12}(f)$. This is mainly due to the fact that $\theta^1_{12}(f)$ is positive for $y^+ < 26$ and hence $C^{12}_{\text{no rot}}(f)$ and the rotational correction are proportional to the difference between the measured values of $\theta^1_{12}(f)$ and $\theta^2_{12}(f)$. The value of $C^{23}_{\text{rot}}(f)$ is least sensitive to both the measured value and the rotational correction. Thus this quantity, rather than the least-squares fit to the data, may be the best estimate of $C_1(f)$ for $y^+ < 26$.

REFERENCES

Bakewell, H. P. & Lumley, J. L. 1967 *Phys. Fluids* **10**, 1880.

Brillouin, L. 1960 *Wave Propagation and Group Velocity*. Academic Press.

Clauser, F. A. 1956 Turbulent boundary layer. *Adv. in Appl. Mech.* **4**, 2.

Cooley, J. W. & Tukey, J. W. 1965 An algorithm for the machine calculation of complex Fourier series. *Math. Comp.* **19**, 297.

Favre, A. J. 1965 *J. Appl. Mech.* **22**, 241.

Grant, H. L. 1958 *J. Fluid Mech.* **4**, 149.

Heidrick, T. R. 1974 Ph.D. dissertation, University of Manitoba.

Heidrick, T. R., Azad, R. S. & Banerjee, S. 1972 In *Turbulence in Liquids* (ed. J. L. Zakin & G. K. Patterson), p. 143. University of Missouri-Rolla Press.

Kármán, Th. von 1931 *Collected Works*, vol. 11, p. 337 (as referred to in Schlichting 1968).

Kim, H. T., Kline, S. J. & Reynolds, W. C. 1968 *Stanford Univ. Rep.* MD-20.

Kim, H. T., Kline, S. J. & Reynolds, W. C. 1971 *J. Fluid Mech.* **50**, 133.

KLEBANOFF, P. S., TIDSTROM, K. D. & SARGENT, L. M. 1962 *J. Fluid Mech.* **12**, 1.

KLINE, S. J., REYNOLDS, W. C., SCHRAUB, F. A. & RUNSTADLER, P. W. 1967 *J. Fluid Mech.* **30**, 741.

KOVASZNAY, L. S. G., KOMODA, H. & VASUDEVA, B. R. 1962 *Proc. Heat Transfer Fluid Mech. Inst.*, p. 1. Stanford University Press.

LAHEY, R. T. & KLINE, S. J. 1971 *Stanford Univ. Rep.* MD-26.

LANDAHL, M. T. 1976 *J. Fluid Mech.* **29**, 441.

LAUFER, J. 1954 *N.A.C.A. Rep.* no. 1174.

MARTIN, G. O. & JOHANSON, L. N. 1965 *A.I.Ch.E. J.* **11**, 29.

MORRISON, W. R. B. 1969 Ph.D. thesis, Dept. Mech. Engng, University of Queensland.

PHILLIPS, O. M. 1967 *J. Fluid Mech.* **27**, 131.

PRANDTL, L. 1926 *Z. angew. Math. Mech.* **15**, 136. (See also *Collected Works*, vol. 11, p. 736.)

ROSHKO, A. 1953 *N.A.C.A. Tech. Note* no. 2913.

SCHLICHTING, H. 1968 *Boundary Layer Theory*. McGraw-Hill.

SHIH, C. S. 1968 *Stat. Res. Service, Can. Dept. Agric., Prog.* 5011.

STEGEN, G. R. & VAN ATTA, C. W. 1970 *J. Fluid Mech.* **42**, 689.

STERNBERG, J. 1967 *Phys. Fluids Suppl.* **10**, S146.

TAYLOR, G. I. 1938 *Proc. Roy. Soc.* A **164**, 476.

TOWNSEND, A. A. 1956 *The Structure of Turbulent Shear Flow*. Cambridge University Press.

TOWNSEND, A. A. 1958 *IUTAM Boundary Layer Res. Symp.* Springer.

TOWNSEND, A. A. 1961 *J. Fluid Mech.* **11**, 97–120.